applied sciences

MDPI

Article

Kinetics of H_2O_2 Decomposition and Bacteria Inactivation in a Continuous-Flow Reactor with a Fixed Bed of Cobalt Ferrite Catalyst

Nazarii Danyliuk [1], Viktor Husak [2], Volodymyra Boichuk [3], Dorota Ziółkowska [4,*], Ivanna Danyliuk [1] and Alexander Shyichuk [1,4]

1 Educational and Scientific Center of Materials Science and Nanotechnology, Vasyl Stefanyk Precarpathian National University, 76018 Ivano-Frankivsk, Ukraine; danyliuk.nazariy@gmail.com (N.D.); ivanna.lapchuk@pnu.edu.ua (I.D.); szyjczuk@pbs.edu.pl (A.S.)
2 Department of Biochemistry and Biotechnology, Vasyl Stefanyk Precarpathian National University, 76018 Ivano-Frankivsk, Ukraine; viktor.husak@pnu.edu.ua
3 Department of Applied Physics and Materials Science, Vasyl Stefanyk Precarpathian National University, 76018 Ivano-Frankivsk, Ukraine; volodymyra.boichuk@pnu.edu.ua
4 Faculty of Chemical Technology and Engineering, Bydgoszcz University of Science and Technology, Seminaryjna 3, 85-326 Bydgoszcz, Poland
* Correspondence: dorota_z@pbs.edu.pl

Featured Application

The developed laboratory-scale flow reactor uses H_2O_2 to generate hydroxyl radicals and inactivate bacteria. This approach is suitable for the construction of decentralized water treatment systems.

Abstract

As a result of the catalytic decomposition of H_2O_2, hydroxyl radicals are produced. Hydroxyl radicals are strong oxidants and effectively inactivate bacteria, ensuring water disinfection without toxic chlorinated organic by-products. The kinetics of bacterial inactivation were studied in a laboratory-scale flow catalytic reactor. A granular cobalt ferrite catalyst was thoroughly characterized using XRD and XRF techniques, SEM with EDS, and Raman spectroscopy. At lower H_2O_2 concentrations, H_2O_2 decomposition follows first-order reaction kinetics. At higher H_2O_2 concentrations, the obtained kinetics lines suggest that the reaction order increases. The kinetics of bacterial inactivation in the developed flow reactor depends largely on the initial number of bacteria. The initial bacterial concentrations in laboratory tests were within the range typical of real river water. A regression model was developed that relates the degree of bacterial inactivation to the initial number of bacteria, the initial H_2O_2 concentration, and the contact time of water with the catalyst.

Keywords: cobalt ferrite; Fenton-like catalyst; water disinfection

Academic Editor: Carmen Zaharia

Received: 2 July 2025
Revised: 20 July 2025
Accepted: 22 July 2025
Published: 23 July 2025

Citation: Danyliuk, N.; Husak, V.; Boichuk, V.; Ziółkowska, D.; Danyliuk, I.; Shyichuk, A. Kinetics of H_2O_2 Decomposition and Bacteria Inactivation in a Continuous-Flow Reactor with a Fixed Bed of Cobalt Ferrite Catalyst. *Appl. Sci.* **2025**, *15*, 8195. https://doi.org/10.3390/app15158195

1. Introduction

The quality of tap water is important for the functioning of households and industry. When the source of a water supply is a river, water quality is determined by both natural factors (geological conditions, forest cover, and climate in the river basin) and anthropogenic factors (pollutions from agriculture, households, industry, hospitals, etc., in the form of sewage and surface runoff) [1]. Common water pollutants include pathogenic bacteria and

viruses, mainly originating from domestic sewage and agricultural activities [1]. A sudden, uncontrolled increase in the number of pathogens may occur as a result of water treatment plant failure, the overflow of the sewage system due to heavy rainfall, and other crisis situations [2]. The microbiological purity of water is usually determined by the content of *Escherichia coli* (*E. coli*) and fecal coliform bacteria.

Disinfection is an important step in the preparation of drinking water and wastewater treatment. A commonly used and economical method of disinfection is chlorination, which effectively inactivates bacteria and other pathogens. However, molecular chlorine reacts with dissolved organic matter to form chlorinated by-products that are hazardous to human health [3,4]. Typical examples of toxic halogenated by-products are trihalomethanes and haloacetic acids [5]. An alternative to chlorination may be ozonation or UV radiation. These techniques are very effective for primary disinfection, but long-lasting chlorine remains superior for secondary disinfection of water distribution systems [4]. The main disadvantage of ozonation and UV radiation is their high energy consumption [6].

Hydroxyl radicals are also very effective disinfectants. Due to their high oxidizing potential, hydroxyl radicals easily damage cell membranes and DNA, leading to the death of bacteria [7]. Compared to chlorine, hydroxyl radicals are more environmentally friendly because they destroy bacteria without leaving toxic by-products. Catalytically generated hydroxyl radicals have been successfully tested on real samples from municipal wastewater treatment plants [8,9]. The Fenton process has been proven to provide effective disinfection, especially when used after coagulation/flocculation of wastewater [9].

Compared to the homogeneous Fenton catalyst, heterogeneous catalysts (Fenton-like catalysts) have the advantage that they can be used for a long time. Fenton-like catalysts effectively produce hydroxyl radicals from hydrogen peroxide [8,10]. Typical Fenton-like catalysts are oxides of transition metals [11]. Among metal oxide catalysts, compounds with a spinel crystal structure are of particular interest due to their adjustable properties [12]. Changing the elemental composition and annealing can cause a transition from the normal spinel structure to the inverse spinel structure. As a result, oxygen vacancies and other structural defects are created that act as catalytic sites [13]. Recently, hydrogen peroxide has been tested for bacterial inactivation in continuous-flow mode using hematite [14] and cobalt ferrite [15] catalysts. The effect of H_2O_2 and inorganic anion concentrations was investigated.

This paper examines in detail the kinetics of H_2O_2 decomposition and bacterial inactivation. Disinfection tests were conducted using bacterial counts similar to those found in natural river water.

2. Materials and Methods

2.1. Reagents

Cobalt(II) chloride hexahydrate (>99%, ACS grade) and iron(III) chloride hexahydrate (>99%, ACS grade) were obtained from Sigma-Aldrich (Saint Louis, MO, USA). Hydrogen peroxide (30% *w*/*v*, AR grade), ammonium metavanadate (≥99.0%, ACS grade), H_2SO_4, and $NaHCO_3$ were obtained from Sfera Sim (Lviv, Ukraine).

2.2. Synthesis and Characterization of the Catalyst

Cobalt ferrite was synthesized by alkaline co-precipitation using carboxymethylcellulose to prevent nanoparticle agglomeration and facilitate pore formation [11]. The desired amounts of iron(III) chloride and cobalt(II) chloride were dissolved in a 1 wt% solution of sodium carboxymethylcellulose, heated to 80–90 °C, and stirred for 30 min. Then, 5 M NaOH solution was added dropwise to a pH of 14, and the resulting suspension was further stirred for 30 min. The formed $CoFe_2O_4$ precipitate was separated using a neodymium

magnet, thoroughly washed, and dried. The obtained powder material was pressed into pellets of 10 mm × 3 mm and sintered at 1150 °C for 6 h. The sintered pellets were then crushed into irregularly shaped grains and sieved. The fraction with a size from 0.8 to 1 mm was used.

The X-ray powder diffraction (XRD) pattern of the cobalt ferrite catalyst was recorded at room temperature using a Shimadzu XRD–7000 X-ray diffractometer (Shimadzu Corporation, Kyoto, Japan) with monochromatic CuKα radiation (λ = 1.5418 Å). The powder samples were scanned from 5° to 65° with a step angle of 0.02° and 2 s per step. XRD analysis was performed using the full-profile Rietveld refinement method implemented in the FullProf software package (ver. January 2018). Peak deconvolution was carried out employing the pseudo-Voigt function.

X-ray fluorescence (XRF) measurements were performed using an EXPERT 3L XRF spectrometer (INAM, Kyiv, Ukraine) with helium flushing. SEM images were recorded using a REMMA-102_02 scanning electron microscope (JCS SELMI, Sumy, Ukraine) operated at an accelerating voltage of 20 kV. An energy-dispersive spectrum (EDS) was recorded at the location where the SEM image was taken.

Raman spectra were recorded using a Bruker Raman Microscope (Billerica, MA, USA) with a 1 mW laser emitting light at a wavelength of 785 nm, a magnification of ×20, an aperture of 50 µm, and 800 scans with a resolution of 1.5 cm^{-1}.

2.3. H_2O_2 Decomposition in Continuous-Flow Mode

The flow reactor is a cylindrical stainless-steel tube with a length of 100 cm and an internal diameter of 12 mm (Figure 1), containing 180 g of cobalt ferrite granules (see Section 2.2). The measured empty volume was 72 mL. The bacterial solution and H_2O_2 solution were pumped using a two-line peristaltic pump with a total flow from 2.5 to 150 mL/min.

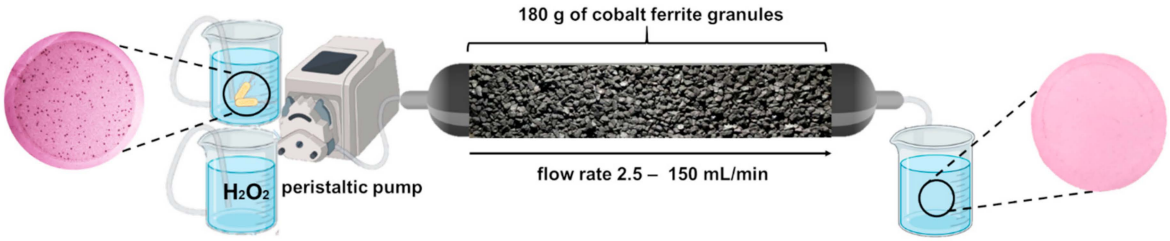

Figure 1. Scheme of the continuous-flow reactor setup.

The concentration of residual H_2O_2 after the reactor was determined using the color reaction with metavanadate in an acidic medium [11,16]. First, 1 mL of the test solution was mixed with 1.5 mL of 5 M H_2SO_4 solution and 1.5 mL of 0.1 M NH_4VO_3, made up to 5 mL with distilled water, and mixed thoroughly. The absorbance at 470 nm was measured within 10 min using a ULAB 102-UV spectrophotometer (Himlaborreactiv, Cherkasy, Ukraine).

2.4. Determination of the Properties of Natural River Water

Natural water samples were taken from the Bystrytsia Nadvirnianska river [17] in February 2025. The source of the Bystrytsia Nadvirnianska river, marked with a blue dot in Figure 2a, is located in the Gorgany massif (Eastern Carpathians). Sampling points are marked with red markers in Figure 2a. River water samples were collected in sterile flasks with a capacity of 0.5 L. Samples for bacterial testing were cultured within 2 h of collection. Chemical parameters were tested within 2 days.

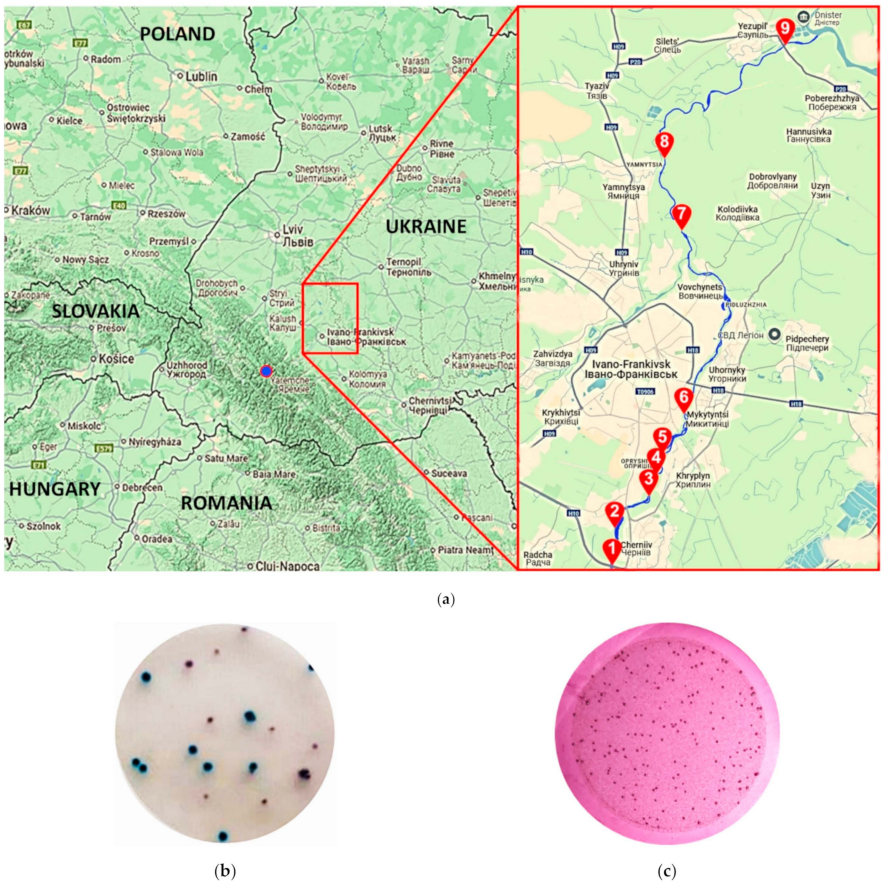

(a)

(b)

(c)

Figure 2. (**a**) River water sampling map. (**b**) Compact Dry EC bacterial test performed on 1 mL of water collected at sampling point no. 5. Dark-blue and -purple spots represent *E. coli* and coliform colonies, respectively. (**c**) Endo agar bacterial test performed on 100 mL of water collected at sampling point no. 6.

The pH and TDS values of the river water were determined using an Apera Instruments PH800 pH meter (Columbus, OH, USA) and a Milwaukee Mi 170 conductometer (Szeged, Hungary). The color of the water samples was determined by measuring absorbance at 411 nm and comparing it with the standard Pt-Co scale [18]. The concentration of Fe^{3+} ions was determined by measuring absorbance at 486 nm after color reaction with thiocyanate anions [19]. Water hardness was determined by measuring absorbance at 606 nm after reaction with Arsenazo III [20].

2.5. Bacterial Count and Disinfection Testing

Bacterial counts were determined using Compact Dry EC chromogenic plates (Shimadzu Diagnostics, Tokyo, Japan) and Endo agar tests (Farmaktiv, Kyiv, Ukraine), which were incubated at 37 ± 1 °C for 24 h. Example test plates are shown in Figure 2b,c. Compact Dry EC plates demonstrate dark-blue and -purple spots corresponding to *E. coli* and coliform colonies, respectively (Figure 2b). Endo agar tests produce dark-red spots indicating the presence of *E. coli* only (Figure 2c).

The disinfection study was performed using the *E.coli* strain ATCC 35218 (Pol-Aura, Morąg, Poland). The stock bacterial suspension was diluted to the desired bacterial number and introduced into the flow reactor using a peristaltic pump. The tested solutions were filtered through nitrocellulose membrane filters (SpectroLab, Kyiv, Ukraine) with a pore diameter of 0.9 μm. The volume of filtered solution was 10 mL or 100 mL in the case of a high or low bacterial concentration, respectively. Inoculated filters were placed on Endo agar and incubated at 37 ± 1 °C for 24 h. Then the grown colonies with a dark-red color

and metallic sheen were counted. The kinetics of bacterial inactivation were modeled using the Python programming language, v. 3.12.

3. Results and Discussion

3.1. Catalyst Characterization

Figure 3 shows SEM images of cobalt ferrite catalyst granules at different magnifications. The granules have irregular shapes and sizes from 0.8 to 1 mm (Figure 3a). The surface of some granules is mechanically damaged (Figure 3a,b). Probably, longer sintering is necessary to provide stronger granules. Increased magnifications (Figure 3c–e) reveal that granules are composed of smaller particles. The smallest particles have sizes ranging from 2 to 0.5 μm (Figure 3f).

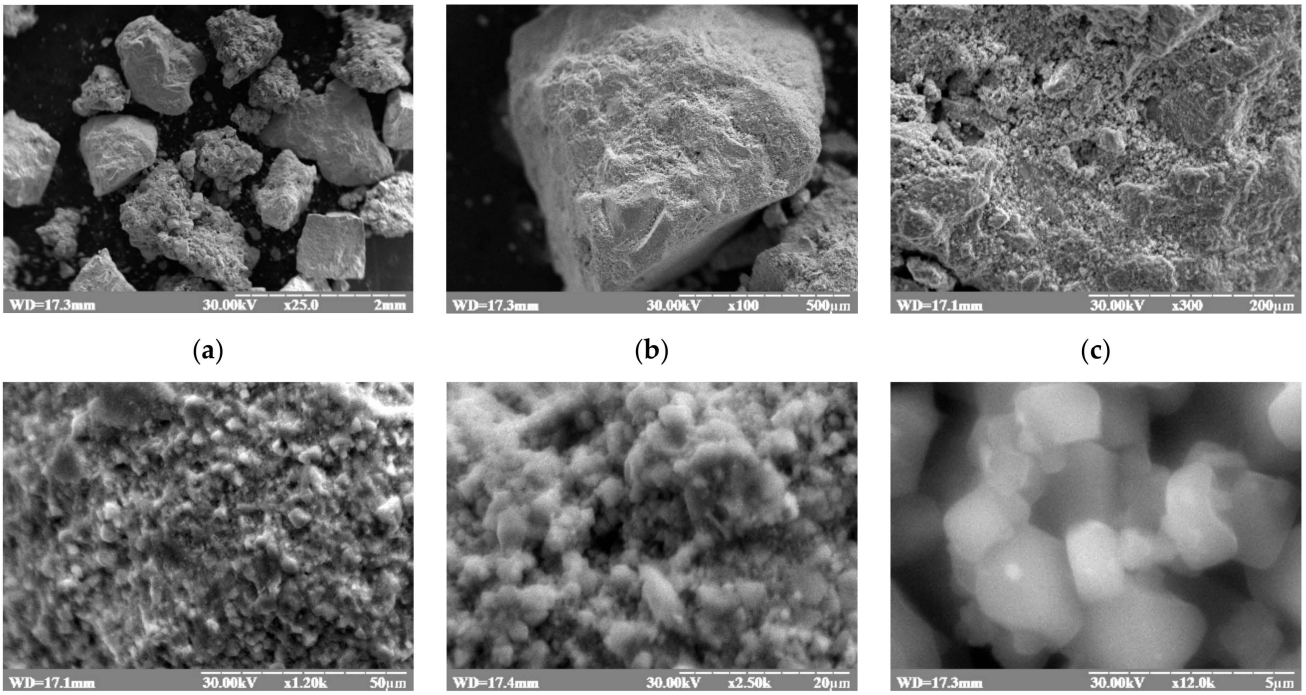

Figure 3. SEM images of catalyst granules at different magnifications (**a**–**f**).

Figure 4a shows the EDS spectrum of the catalyst surface. The recorded peaks belong to cobalt, iron, and oxygen atoms. No peaks of other atoms are visible, indicating that the tested material is a mixed Co-Fe oxide. Figure 4b shows the XRF spectrum of the tested catalyst. This spectrum contains only peaks of cobalt and iron. The XRF method is more sensitive than EDS and allows for the detection of trace elements, especially those with high atomic mass. Therefore, the absence of other peaks in the XRF spectrum confirms the high purity of the synthesized catalyst material.

Both the XRF and EDS techniques also allow the quantitative determination of elemental composition. The intensity of EDS peaks allowed the determination of the mass content of Fe_2O_3 and CoO, which is 63.4% and 36.6%, respectively. Therefore, the resulting formula of mixed cobalt–iron oxide is $Co_{1.18}Fe_{1.92}O_{4.06}$. In turn, the intensity of XRF peaks allowed the determination of the mass ratio of Co to Fe, which is 24.4 to 43.4. Therefore, the resulting formula is $Co_{1.05}Fe_{1.96}O_4$. Both obtained formulas are consistent with each other and correspond well to the general formula of cobalt ferrite, $CoFe_2O_4$.

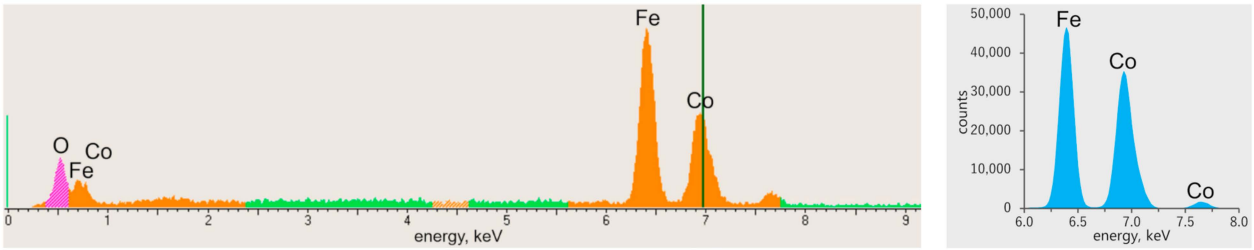

(**a**) (**b**)

Figure 4. (**a**) EDS and (**b**) XRF spectra of the cobalt ferrite catalyst material. The color meanings are as follows: green—background, orange—transition metals, pink—non-metals.

Figure 5a shows the X-ray diffraction pattern of the synthesized catalyst. The narrow reflections indicate the highly crystalline nature of the sample. The obtained diffraction pattern agrees well with the JCPDS #74-2403 pattern, confirming the formation of a single-phase cobalt ferrite without impurity phases. The most intense diffraction peak corresponds to the (311) plane. The other reflections are also characteristic of the standard cubic spinel structure and belong to the (111), (220), (400), (511), and (440) planes (Figure 5).

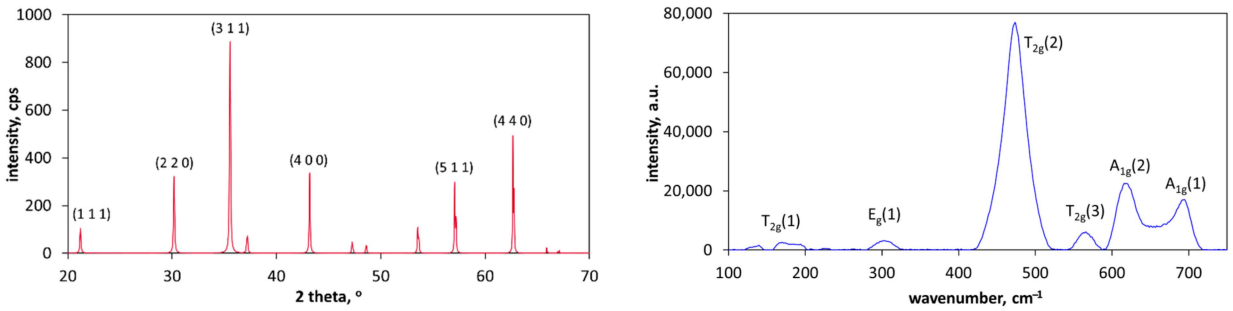

(**a**) (**b**)

Figure 5. (**a**) X-ray diffraction pattern and (**b**) Raman spectrum of the tested catalyst.

The average crystallite size (coherent scattering area, DS) was calculated using the Scherrer formula:

$$DS = 0.89\,\lambda/\beta\,\cos\theta, \quad (1)$$

where λ is the X-ray wavelength (here, λ = 1.5406 Å), θ is the Bragg angle, and β is the full width at half maximum (FWHM) for the most intense (311) reflection in the XRD pattern [21].

Rietveld refinement and Scherrer calculations showed that the average crystallite size is about 80 nm. This value is higher than the typical values recorded for as-synthesized cobalt ferrite samples [22]. The observed difference is because the tested catalyst was sintered at a high temperature of 1100 °C. The lattice parameter was calculated to be 8.38 Å. This value is consistent with the literature data regarding the lattice parameter of cobalt ferrite [23,24].

The Raman spectrum (Figure 5b) is typical for ferrite spinels [25,26]. The characteristic peaks were assigned to the corresponding vibrational modes of the metal–oxygen bonds in the spinel lattice (Figure 5b). Therefore, the presented XRD pattern (Figure 5a) and Raman spectrum (Figure 5b) confirm that the synthesized catalyst is a cobalt ferrite spinel.

3.2. H_2O_2 Decomposition Kinetics

Figure 6 illustrates the kinetics of H_2O_2 decomposition in continuous-flow mode, determined with varying initial H_2O_2 concentrations. The extent of H_2O_2 decomposition is approximately 10–15% of the initial concentration (Figure 6a,b). The low degree of H_2O_2 decomposition is due to the relatively short contact time of the solution with the catalyst in the fixed bed, which is about 30 min.

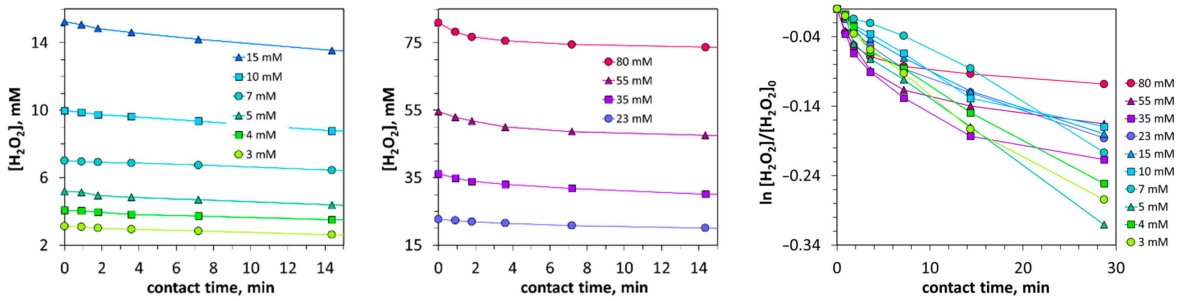

(**a**) (**b**) (**c**)

Figure 6. The kinetics of H_2O_2 decomposition in the flow reactor at different initial concentrations of H_2O_2. (**a**,**b**) The changes in H_2O_2 concentration over time. (**c**) The changes in H_2O_2 concentration plotted on a logarithmic scale.

Figure 6c shows the kinetics lines plotted on a logarithmic scale. In the case where the initial H_2O_2 concentrations are in the range from 3 to 15 mM, the plots are linear. This fact indicates that the H_2O_2 decomposition kinetics follow the kinetics of a first-order reaction. In the case where the initial H_2O_2 concentration exceeds the threshold value of 23 mM, the graphs become nonlinear (Figure 6c). This fact indicates that the decomposition of H_2O_2 does not fit the kinetics of a first-order reaction. The graphs are concave downward, suggesting that the reaction order is higher than one.

We observed a similar effect in our previous work [22] and explained it by side reactions. The hydroxyl radicals formed react with hydrogen peroxide, leading to the formation of hydroperoxide radicals (Equation (2)). The hydroperoxide radicals then react with each other to form O_2 and H_2O_2 (Equations (3) and (4)). The rate of the side reaction (2) increases at higher initial H_2O_2 concentrations. Therefore, the kinetic plots on a logarithmic scale deviate from linearity at higher initial H_2O_2 concentrations.

$$HO^{\bullet} + H_2O_2 \rightarrow HOO^{\bullet} + H_2O \quad (2)$$

$$HOO^{\bullet} \leftrightarrow H^+ + O_2^{\bullet -} \quad (3)$$

$$HOO^{\bullet} + H^+ + O_2^{\bullet -} \rightarrow O_2 + H_2O_2 \quad (4)$$

3.3. Bacterial Inactivation

3.3.1. Testing Natural River Water for Bacterial Contamination

Figure 7 shows the physicochemical and microbiological characteristics of water in the Bystrytsia river. The pH values tend to increase slightly downstream (Figure 7a) and range from 8.20 to 8.65, which is generally acceptable for drinking water [27]. Increased water pH values may have natural or anthropogenic causes, i.e., leaching of alkali salts from the riverbed and surface runoff from agricultural areas. In turn, changes in the TDS parameter are likely caused by anthropogenic factors (Figure 7a). The highest TDS values occur at points 5–7, i.e., within and below the urban area, indicating human influence. A slight increase in TDS was also recorded near the smaller town of Yezupil (point 9 in Figures 2a and 7a). The

WHO does not set any guidelines for TDS in drinking water [28]. Measured TDS values range from 112 to 166 ppm (Figure 7a) and are lower than the level of 600 ppm considered good for water taste.

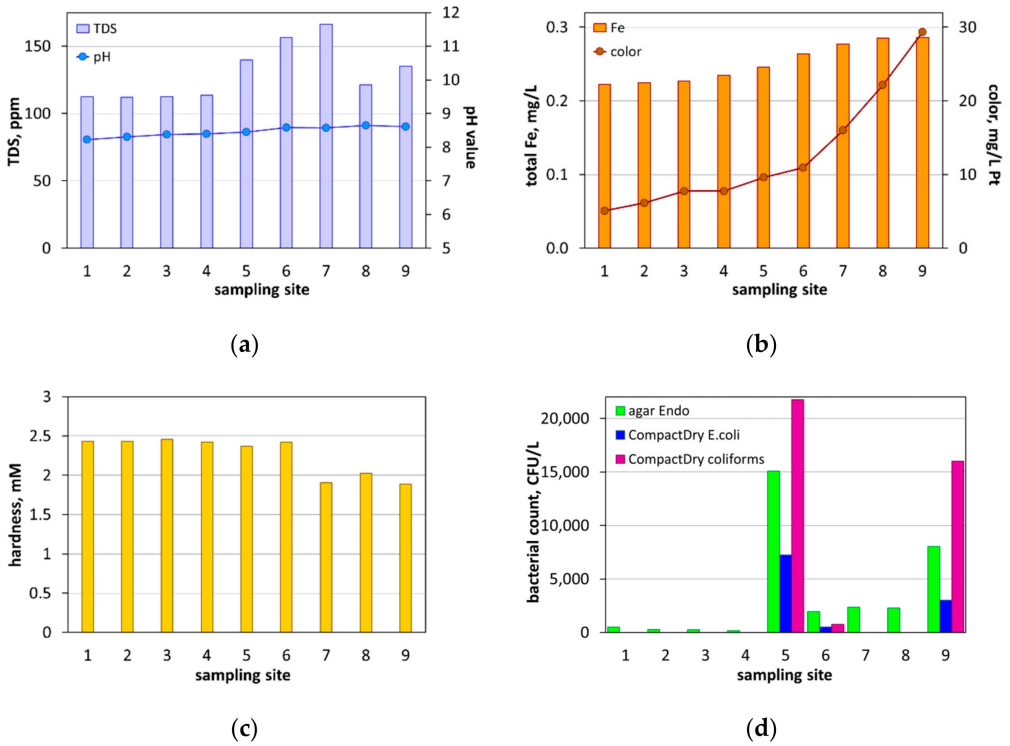

Figure 7. Characteristics of natural water taken from the Bystrytsia river: (**a**) pH value and total dissolved salt, (**b**) water color and iron concentration, (**c**) total hardness, and (**d**) the number of bacteria.

The color of the river water tends to increase, especially at points 5–9 (Figure 7b). The observed increase in water color may be caused by the leaching of humic acids and iron ions from the soil. An increase in iron concentrations was also observed (Figure 7b), which confirms the above explanation. The iron content increases to almost 0.3 mg/L, which the WHO considers a critical level [28]. The recorded iron concentrations are not dangerous, but indicate the need for further monitoring.

Figure 7c shows the water hardness values corresponding to the total content of calcium and magnesium ions. At points 1–6, the river water has a hardness of approximately 2.4 mM. Further along the river, the hardness decreases to 1.9–2 mM (Figure 7c). This effect is caused by the inflow of another river (Bystrytsia Solotvynska) between sampling points 6 and 7 (Figure 2a). Comparison of Figure 7a,c suggests that the TDS changes are not due to calcium and magnesium ions. The changes in TDS are probably caused by sodium ions of anthropogenic origin.

Figure 7d shows the number of bacteria at the different sampling points indicated in Figure 2a. The number of *E. coli* bacteria was determined using two different tests: the classic Endo agar test and the Compact Dry test (Section 2.5). The two tests were found to have different sensitivities, with the Endo agar test detecting approximately twice as many bacteria as the Compact Dry test (Figure 7d). On the other hand, the Compact Dry test has the advantage of providing information on both the *E. coli* count and the total coliform count (Figure 2b).

Typically, microbiological contamination of rivers varies significantly depending on the sampling location and time. For example, the *E. coli* count in a small river in Germany ranges from 1×10^3 to 4.7×10^4 CFU/L [2]. High population density and a hot climate

can cause very high bacterial loads. An example is the main river of Ecuador, where the number of *E. coli* bacteria ranges from 5×10^4 to 2.5×10^5 CFU/L [1]. In the Bystrytsia Nadvirnianska river, the bacterial count at sampling points 1–3 (above the city) ranges from 240 to 500 CFU/L (Figures 2a and 7d). The reason for such low bacterial contamination is the fact that the river flows through rural areas. However, the river in urban areas has a much higher bacterial load. The highest number of bacteria was recorded at point 5, located in the city of Ivano-Frankivsk (Figures 2a and 7d). Further downstream, *E. coli* and coliform levels decline, likely due to dilution. Another increase in the number of bacteria was recorded at point 9 (Figure 7d), which is located in the smaller town of Yezupil, right next to the river (Figure 2a).

Recorded spikes in bacterial counts suggest the presence of local sources of fecal contamination (e.g., discharges of domestic or animal sewage). Fecal bacteria pose a particularly high risk to human health, especially in areas used for recreational purposes. Exfiltration of sewage from sewage systems into the ground and its subsequent leaching into surface waters can lead to contamination of river water with fecal bacteria. The presence of both treated and untreated sewage discharge points in the river basin is one of the reasons for the uneven distribution of bacterial concentrations in river water. This is confirmed by extensive studies carried out in the basin of the Danube River, which is the second longest river in Europe [29]. Similar patterns were observed in the small river Swist in Germany, where *E. coli* counts at sampling points located in a relatively small area varied by a factor of 50 [2]. This is due to differences in land use, i.e., the presence of urban agglomerations, agricultural areas, bathing areas, etc.

In this study, the increased number of bacteria at sampling point 9 (Figure 7d) may be due to poor agricultural waste management practices or leaks in the sewage system in the small town of Yezupil (Figure 2a) [30]. The sewage system in a small town is based more on cesspools than on a central sewage system. Therefore, there may be point sources of discharge of untreated sewage. Methods for detecting and distinguishing sources (human and animal) of fecal bacteria in water are constantly being improved [30]. Exfiltration phenomena are modeled to predict water contamination [31], also using in situ measurements [32].

It can be stated that the inhabitants of the Bystrytsia river basin are supplied with good-quality water. The registered local increase in bacterial loads does not cause any significant deterioration of water parameters.

3.3.2. Inactivation of Bacteria in a Flow Reactor

The assessment of river water for bacterial counts (Section 3.3.1) provided sufficient information to plan experiments on bacterial inactivation in the flow reactor. The initial bacterial load was in a realistic range of 1200 to 54,000 CFU/L (Figure 8a). Figure 8a shows the changes in the number of bacteria at the initial stage of inactivation (7 min). Figure 8b,c show the relative survival of bacteria (N/N_0) over the full time range (28 min).

At a low initial bacterial load (1200–6900 CFU/L), a rapid and significant reduction in bacterial counts is observed within the first minute of contact (Figure 8a). The relative survival of bacteria also decreases rapidly within the first minute of inactivation (Figure 8b). After 10 min, the bacteria are almost completely inactivated.

However, bacteria survive better at higher initial concentrations (Figure 8c). At high initial bacterial loads ($\geq$9000 CFU/L), bacterial inactivation becomes slow and incomplete (Figure 8a). Even after 28 min, a significant portion of the bacterial cells remain viable, especially at $N_0 > 40{,}000$ CFU/L (Figure 8c). There is a clear concentration dependence: the higher the initial bacterial count, the less effective the inactivation (Figure 8c).

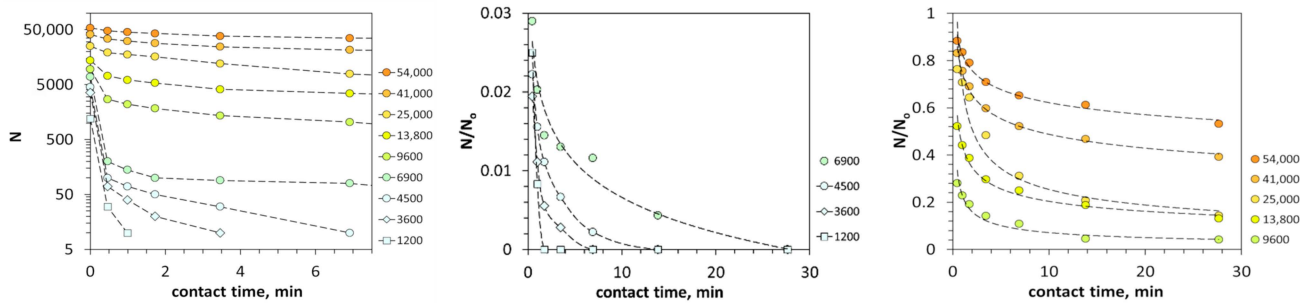

(**a**) (**b**) (**c**)

Figure 8. Bacterial inactivation kinetics at different initial bacterial concentrations (expressed in CFU/L) in the presence of 10 mM hydrogen peroxide: (**a**) absolute survival (N) vs. contact time; (**b**) normalized survival (N/N_0) as a function of time for low initial bacterial concentrations; (**c**) normalized survival (N/N_0) as a function of time for high initial bacterial concentrations.

Figure 8b,c clearly show that the kinetics of bacterial inactivation are highly nonlinear. Bacterial inactivation appears to occur in two stages: first, there is a rapid initial decline in bacterial numbers, followed by a slower second stage. There are several possible causes for the slow inactivation phase. The obvious cause is the increasing number of dead bacteria, whose damaged cells lose their internal cytoplasmic components. The washed-out molecules react with hydroxyl radicals, which reduces the number of active radicals and slows down the rate of bacterial inactivation. Another reason for the slowdown in bacterial inactivation is the fact that the bacterial population includes bacteria with varying resistance to aggressive radicals. Some bacteria have better defense mechanisms and can reproduce within about 30 min of the experiment, resulting in a lower inactivation rate.

An additional inhibiting effect may occur as a result of the formation of a biofilm on the catalyst surface. Figure 9 illustrates how increasing the bacterial concentration facilitates biofilm formation in the catalyst bed. At low bacterial concentrations (left side of Figure 9), the catalyst surface remains clean and exposed to hydrogen peroxide, allowing continuous formation of reactive oxygen species. The obvious effect is poor bacterial survival. In contrast, at higher bacterial concentrations (right side of Figure 9), bacterial cells colonize the catalyst surface and begin forming a protective biofilm matrix. This biofilm is mainly composed of polysaccharides, proteins, and extracellular nucleic acids [33,34]. These extracellular polymeric substances significantly increase the adhesion of bacterial cells to the catalyst surface. The biofilm progressively envelops the catalyst surface, preventing its contact with hydrogen peroxide, thus reducing the number of radicals and facilitating bacterial survival. Similar protective mechanisms have been observed in *Escherichia coli* and *Pseudomonas aeruginosa*, where shielding with extracellular polymeric substances increases the survival of bacteria under conditions of oxidative and chemical stress [33]. This survival strategy in various Gram-negative bacteria is controlled by chemosensory signaling systems, allowing them to adapt to environmental stresses [34,35]. Biofilm-based shielding may explain the observed stabilization of bacterial viability at higher initial bacterial counts. A similar phenomenon of physical covering of the catalyst surface with a dense biofilm is known as biofouling [36,37]. Therefore, the formation of bacterial biofilms on the catalyst surface may represent a synergistic effect: improving microbial persistence while simultaneously reducing ROS formation.

Figure 10 shows a contour map illustrating the dependence of the inactivation efficiency on the initial number of bacteria and the contact time with 10 mM H_2O_2. The map shows three areas of catalyst performance: the effective area, marked in dark blue, the transition area, marked in light blue, and the ineffective area, marked in orange. The

effective area with a pronounced bactericidal effect corresponds to an initial bacterial load below 13,800 CFU/L and a contact time of over 7 min. The survival rate is below 25%, which is confirmed by the graphs in Figure 8c. The low concentrations of 1200–6900 CFU/L require only 2–4 min to achieve almost complete inactivation (Figures 8b and 10).

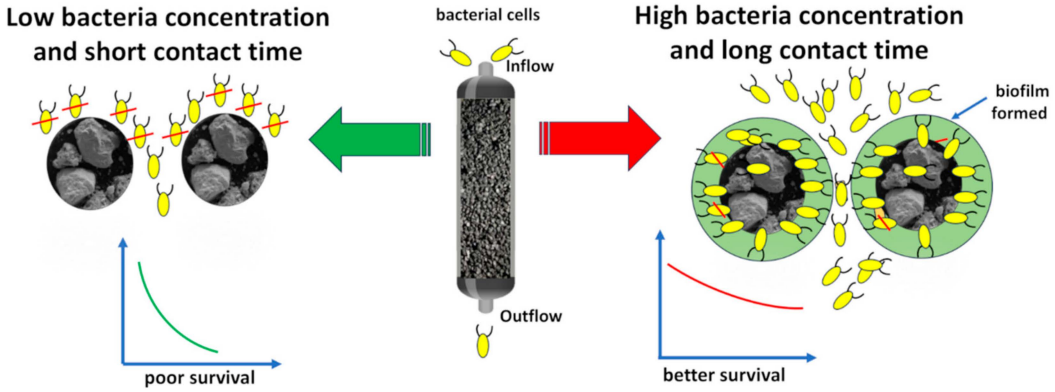

Figure 9. Schematic representation of bacterial survival and biofilm formation in a catalytic reactor with different initial bacterial loads.

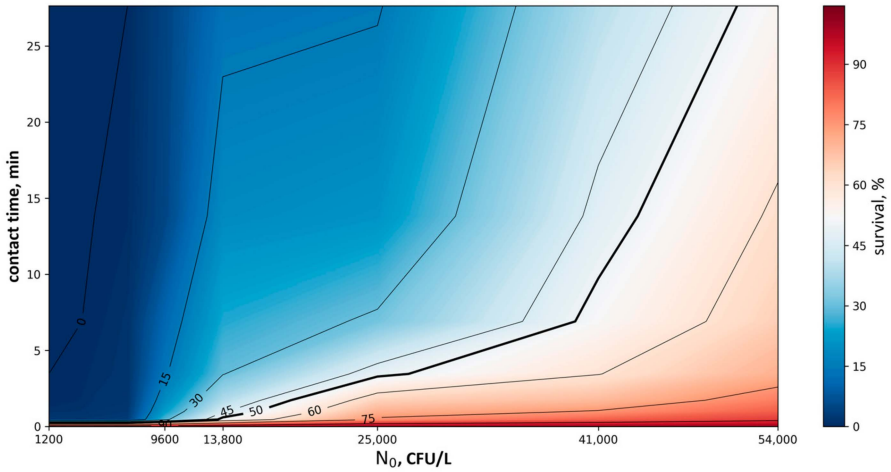

Figure 10. Contour map of bacterial survival depending on the initial number of bacteria and contact time. The thick black line indicates 50% survival.

Partial inactivation of bacteria is observed in the transition area (Figure 10). The typical initial bacterial load here is 13,800–25,000 CFU/L. To achieve a survival level below 30%, longer exposure (up to 10 min) is necessary. This indicates a time-dependent effect of H_2O_2 at a medium microbial load.

The ineffective area is observed at an initial bacterial load above 41,000 CFU/L (Figure 10). At such a high concentration of bacteria, H_2O_2 is not able to completely inactivate them. A high survival rate (>30%) is observed even after a long contact time (28 min).

The contour map in Figure 10 clearly shows the strong dependence of H_2O_2 effectiveness on the initial concentration of bacteria and the contact time. Optimal conditions for disinfection are as follows: a low concentration of bacteria and a contact time longer than 5 min. At high initial bacterial loads (25,000–54,000 CFU/L), the disinfection effect of H_2O_2 is rather limited. To enhance the disinfection effect, a higher concentration of H_2O_2 or a more effective catalyst can be used.

The modeling of bacterial survival under the influence of H_2O_2 was performed taking into account two variables: contact time and initial bacterial concentration. The applied

model is a second-order exponential decay integrated with a logarithmic dependence on the initial bacterial concentration:

$$N(t, N_0) = a \cdot e^{-bt} + c + d \cdot \ln(N_0) \quad (5)$$

where $N(t, N_0)$ is the predicted number of live bacteria (CFU/L) at contact time t (min) and an initial number of bacteria N_0 (CFU/L); a, b, c, and d are model parameters determined by fitting the model equation to the experimental values. In the application of the numerical values of the model parameters, the equation is as follows:

$$N(t, N_0) = -2.6 \times 10^7 \cdot e^{0.0000113 \cdot t} + 2.6 \times 10^7 + 9833 \cdot \ln(N_0) \quad (6)$$

This model describes a nonlinear decrease in bacterial survival over time with an increasing initial bacterial concentration (Figure 11a). The exponential component $2.6 \times 10^7 \cdot e^{0.0000113 \cdot t}$ reflects the time-dependent dynamics of bacterial inactivation, especially in the early phase. The logarithmic expression $9833 \cdot \ln(N_0)$ takes into account the fact that increasing the concentration of bacteria has an inhibitory effect on the inactivation of bacteria. In other words, an increase in the initial concentration of bacteria produces a leveling effect. The R^2 value for this model is 0.66, which means that it is a sufficient approximation of the experimental data. The relatively low R^2 value may be due to the sensitivity of the model to the initial bacterial count, which varies widely from 1200 to 54,000 CFU/L.

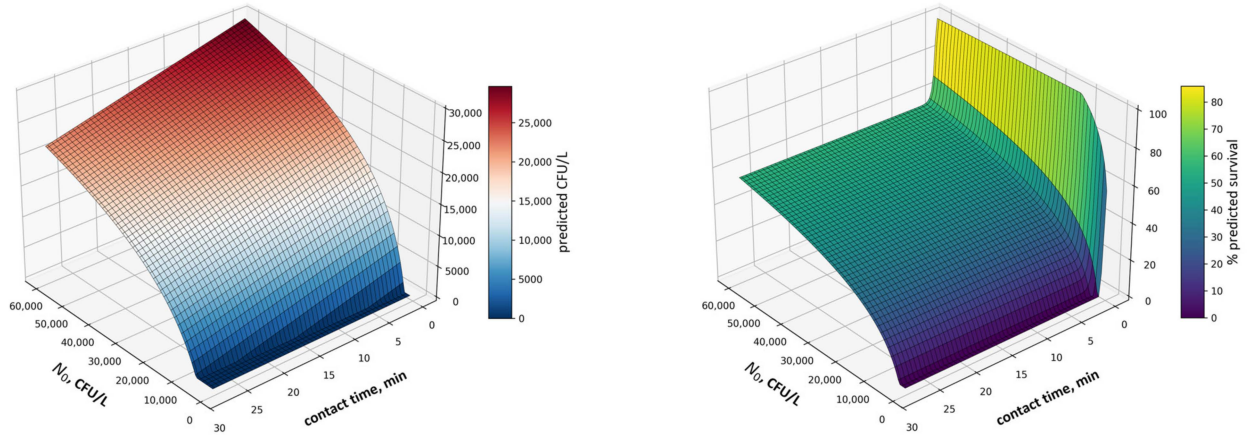

Figure 11. 3D surface plots illustrating predicted bacterial survival as a function of contact time and initial bacterial concentration, based on (**a**) Equation (6) and (**b**) Equation (8).

To limit the influence of absolute values and ensure comparability of data, all experimental values were normalized to percentages relative to the initial bacterial count, defined as 100%. To fit the experimental values of the relative survival rate, the same second-order exponential decay model with logarithmic adjustment was used:

$$R(t, N_0) = v \cdot e^{-xt} + y + z \cdot \ln(N_0) \quad (7)$$

where $R(t, N_0)$ is the predicted relative survival rate (%), t is the contact time (min), N_0 is the initial bacteria count (CFU/L), and v, x, y, and z are the empirical model parameters. The fitting of the model equation to the experimental values yielded the parameter values given in Equation (8):

$$R(t, N_0) = 77.33 \cdot e^{-3.01 \cdot t} - 148.86 + 18.57 \cdot \ln(N_0) \quad (8)$$

The model surface (Figure 11b) shows characteristic features: an exponential decline in bacterial survival over time and a nonlinear, logarithmic decrease in efficiency with increasing initial bacterial numbers. At high initial bacterial numbers (≥25,000–54,000 CFU/L), a clear flattening of the model surface is visible, indicating that a plateau of bactericidal effectiveness has been reached. The model fits the experimental data well (R^2 = 0.82) and allows for reliable predictions within the tested values of contact time and initial bacterial count. The high values of Akaike (AIC = 403.27) and Bayesian (BIC = 412.38) information criteria also confirm the high quality of Model Equation (8). Other models tested (Weibull, logistic, polynomial) have significantly worse performance.

The model combining a second-order exponential decay with a logarithmic adjustment describes well the bactericidal effect of H_2O_2 in the flow catalytic reactor. This model can be used to estimate the time required for effective water disinfection depending on the initial bacterial count. However, the effectiveness of the catalytic reactor also depends on the temperature, concentration of H_2O_2 used, pH, and ions present in the aqueous matrix. Therefore, this model is rather a first step. It is necessary to develop more detailed models that would take into account the influence of the above-mentioned parameters.

4. Conclusions

The use of hydroxyl radicals as a disinfectant is an environmentally friendly approach to water disinfection. A laboratory-scale flow reactor has been designed to produce hydroxyl radicals and inactivate bacteria. The tubular reactor was filled with a previously synthesized catalyst based on cobalt ferrite. Detailed analyses by XRD, XRF, EDS, and Raman spectroscopy showed that the obtained cobalt ferrite is a single-phase spinel with the formula $Co_{1.05}Fe_{1.96}O_4$. The packed-bed catalytic reactor was tested for H_2O_2 decomposition over a wide range of concentrations, from 3 to 80 mM. At low H_2O_2 concentrations, the decomposition follows the kinetics of a first-order reaction. The reaction order likely increases with increasing H_2O_2 concentrations above 10 mM. The synthesized catalyst is stable and remains active for a long time. During the tests, the catalytic reactor operated for over 2000 h without any performance degradation.

The effectiveness of water disinfection was tested in a wide range of initial bacterial concentrations. The initial bacterial counts for testing were selected based on analysis of water from a nearby medium-sized river. The river flows through rural and urbanized areas, providing a source of water for the municipal water supply system. In water disinfection studies, the effect of contact time on reactor efficiency was investigated. It was found that the kinetics and efficiency of bacterial inactivation depend significantly on the initial bacterial concentration. At low bacterial concentrations (below 13,800 CFU/L), rapid and almost complete inactivation of bacteria was observed. In the case of high bacterial concentrations (≥25,000 CFU/L), the bactericidal effectiveness of H_2O_2 decreased. The limited concentration of bacteria that can be effectively inactivated makes the developed method less favorable compared to other disinfection methods, such as chlorination or ozonation. However, the efficiency of the catalytic reactor can be improved by using a more active catalyst that provides deeper decomposition of H_2O_2 and thus produces more hydroxyl radicals.

A regression model was obtained that relates the number of surviving bacteria to their initial number and the time of contact with the catalyst. The conclusion is that the proposed flow reactor can be used for disinfecting water with a moderate bacterial load. Further research is needed to optimize operating parameters and increase disinfection effectiveness.

Author Contributions: Conceptualization, A.S.; methodology, I.D., N.D. and V.H.; software, V.H.; investigation, I.D., N.D., V.B. and V.H.; data curation, N.D.; writing—original draft preparation, A.S., V.B., V.H. and D.Z.; writing—review and editing, A.S. and D.Z.; visualization, D.Z. and V.H.;

funding acquisition, D.Z. and A.S. All authors have read and agreed to the published version of the manuscript.

Funding: This work was supported by the Ministry of Education and Science of Ukraine (project number 0124U000479).

Institutional Review Board Statement: Not applicable.

Informed Consent Statement: Not applicable.

Data Availability Statement: The original contributions presented in this study are included in the article. Further inquiries can be directed to the corresponding author.

Conflicts of Interest: The authors declare no conflicts of interest. The funders had no role in the design of the study; in the collection, analyses, or interpretation of data; in the writing of the manuscript; or in the decision to publish the results.

Abbreviations

The following abbreviations are used in this manuscript:

CFU	Colony-forming unit
EDS	Energy-dispersive X-ray spectroscopy
SEM	Scanning electron microscopy
ROS	Reactive oxygen species
TDS	Total dissolved solids
WHO	World Health Organization
XRD	X-ray diffraction
XRF	X-ray fluorescence

References

1. Anh, N.T.; Can, L.D.; Nhan, N.T.; Schmalz, B.; Le Luu, T. Influences of key factors on river water quality in urban and rural areas: A review. *Case Stud. Chem. Environ. Eng.* **2023**, *8*, 100424. [CrossRef]
2. Essert, S.M.; Zacharias, N.; Precht, T.; Pankratz, D.; Funken, K.; Mutters, N.T.; Kistemann, T.; Schreiber, C. Persistence of MRSA and ESBL-producing *E. coli* and *K. oxytoca* in river water. *Hyg. Environ. Health Adv.* **2023**, *7*, 100072. [CrossRef]
3. Mazhar, M.A.; Madhav, S.; Ahmed, S.; Kumar, P.; Springer, C. Drinking Water Chlorination and Disinfection by-Products: Formation, History, and Regulations. In *Drinking Water Disinfection By-Products*; Springer Nature: Cham, Switzerland, 2024; pp. 21–34. [CrossRef]
4. Mazhar, M.A.; Khan, N.A.; Ahmed, S.; Khan, A.H.; Hussain, A.; Rahisuddin; Changani, F.; Yousefi, M.; Ahmadi, S.; Vambol, V. Chlorination disinfection by-products in municipal drinking water—A review. *J. Clean. Prod.* **2020**, *273*, 123159. [CrossRef]
5. Zheng, W.; Chen, Y.; Zhang, J.; Peng, X.; Xu, P.; Niu, Y.; Dong, B. Control of chlorination disinfection by-products in drinking water by combined nanofiltration process: A case study with trihalomethanes and haloacetic acids. *Chemosphere* **2024**, *358*, 142121. [CrossRef]
6. Demir, M.Z.; Guven, H.; Ersahin, M.E.; Ozgun, H.; Pasaoglu, M.E.; Koyuncu, I. Comparative Life Cycle Assessment of Four Municipal Water Disinfection Methods. *Sustainability* **2024**, *16*, 6104. [CrossRef]
7. Afitiri, A.-R.; Appah Aram, S.; Martienssen, M. Systematic review of the effects of advanced oxidation processes integration with solar water disinfection for improved drinking water production. *Waste Manag. Bull.* **2024**, *1*, 52–59. [CrossRef]
8. Blanco-Canella, P.; Lama, G.; Sanromán, M.A.; Pazos, M. Disinfection through Advance Oxidation Processes: Optimization and Application on Real Wastewater Matrices. *Toxics* **2022**, *10*, 512. [CrossRef] [PubMed]
9. Venâncio, J.P.F.; Ribeirinho-Soares, S.; Lopes, L.C.; Madeira, L.M.; Nunes, O.C.; Rodrigues, C.S.D. Disinfection of treated urban effluents for reuse by combination of coagulation/flocculation and Fenton processes. *Environ. Res.* **2023**, *218*, 115028. [CrossRef] [PubMed]
10. Wang, J.L.; Xu, L.J. Advanced Oxidation Processes for Wastewater Treatment: Formation of Hydroxyl Radical and Application. *Crit. Rev. Environ. Sci. Technol.* **2012**, *42*, 251–325. [CrossRef]
11. Tatarchuk, T.; Bilovol, V.; Shyichuk, A.; Danyliuk, I.; Sokołowski, K.; Gajewska, M. Mesoporous Co-Mn ferrites as highly radical-forming catalysts for wet peroxide oxidation of 4-nitrophenol. *App. Surf. Sci.* **2025**, *690*, 162610. [CrossRef]
12. Tatarchuk, T.; Shyichuk, A.; Naushad, M.; Danyliuk, N.; Lapchuk, I. Copper-substituted magnetite as a Fenton-like catalyst boosted with electromagnetic heating. *J. Water Process Eng.* **2024**, *60*, 105170. [CrossRef]

13. Tatarchuk, T. Studying the Defects in Spinel Compounds: Discovery, Formation Mechanisms, Classification, and Influence on Catalytic Properties. *Nanomaterials* **2024**, *14*, 1640. [CrossRef]
14. Tatarchuk, T.; Shyichuk, A.; Danyliuk, N.; Lapchuk, I.; Macyk, W. Water disinfection using hydrogen peroxide with fixed bed hematite catalyst—Kinetic and activity studies. *Environ. Sci. Pollut. Res.* **2024**, *31*, 26592–26605. [CrossRef]
15. Tatarchuk, T.; Shyichuk, A.; Danyliuk, N.; Lapchuk, I.; Husak, V.; Macyk, W. Fenton-like water disinfection using fixed-bed reactor filled with a $CoFe_2O_4$ catalyst: Mechanisms, the impact of anions, electromagnetic heating, and toxicity evaluation. *Sep. Purif. Technol.* **2024**, *348*, 127748. [CrossRef]
16. Nogueira, R.; Oliveira, M.; Paterlini, W. Simple and fast spectrophotometric determination of H_2O_2 in photo-Fenton reactions using metavanadate. *Talanta* **2005**, *66*, 86–91. [CrossRef] [PubMed]
17. Bystrytsia Nadvirnianska. Available online: https://en.wikipedia.org/wiki/Bystrytsia_Nadvirnianska (accessed on 30 June 2025).
18. Hongve, D.; Akesson, G. Spectrophotometric determination of water colour in hazen units. *Water Res.* **1996**, *30*, 2771–2775. [CrossRef]
19. Kougia, E.; Ioannou, E.; Roussis, V.; Tzovenis, I.; Chentir, I.; Markou, G. Iron (Fe) biofortification of *Arthrospira platensis*: Effects on growth, biochemical composition and in vitro iron bioaccessibility. *Algal Res.* **2023**, *70*, 103016. [CrossRef]
20. Tazin, N.; Patel, D.; Lambert, C.J.; Shad, M.H.M.; Campbell, J.; Gale, B.K. Automated passive serial dilution microfluidic chip for calcium quantification based on the Arsenazo III method. *Sens. Diagn.* **2022**, *1*, 810–820. [CrossRef]
21. Tatarchuk, T.; Danyliuk, N.; Shyichuk, A.; Kotsyubynsky, V.; Lapchuk, I.; Mandzyuk, V. Green synthesis of cobalt ferrite using grape extract: The impact of cation distribution and inversion degree on the catalytic activity in the decomposition of hydrogen peroxide. *Emergent Mater.* **2022**, *5*, 89–103. [CrossRef]
22. Tatarchuk, T.; Shyichuk, A.; Danyliuk, N.; Naushad, M.; Kotsyubynsky, V.; Boychuk, V. Cobalt ferrite as an electromagnetically boosted metal oxide hetero-Fenton catalyst for water treatment. *Chemosphere* **2023**, *326*, 138364. [CrossRef]
23. Liaskovska, M.; Tatarchuk, T.; Kotsyubynsky, V. Green Synthesis of Cobalt–Zinc Ferrites and Their Activity in Dye Elimination via Adsorption and Catalytic Wet Peroxide Oxidation. *Metals* **2025**, *15*, 44. [CrossRef]
24. Thang, P.D.; Rijnders, G.; Blank, D.H.A. Spinel cobalt ferrite by complexometric synthesis. *J. Magn. Magn. Mater.* **2005**, *295*, 251–256. [CrossRef]
25. Anchal; Sarita; Jakhar, N.; Alvi, P.A.; Choudhary, B.L. Comprehensive analysis of Cu-doped $CoFe_2O_4$ nanocrystals: Structural, morphological, optoelectronic, and magnetic properties. *Adv. Powder Technol.* **2025**, *36*, 104748. [CrossRef]
26. Alfonso-González, J.G.; Granja-Banguera, C.P.; Morales-Morales, J.A.; Dector, A. A Facile Glycerol-Assisted Synthesis of Low-Cu^{2+}-Doped $CoFe_2O_4$ for Electrochemical Sensing of Acetaminophen. *Biosensors* **2023**, *13*, 997. [CrossRef] [PubMed]
27. Health Canada. *Guidelines for Canadian Drinking Water Quality: Guideline Technical Document—pH*; Health Canada: Ottawa, ON, Canada, 2016.
28. World Health Organization. *Guidelines for Drinking-Water Quality: Fourth Edition Incorporating the First Addendum*; World Health Organization: Geneva, Switzerland, 2017.
29. Kirschner, A.K.T.; Schachner-Groehs, I.; Kavka, G.; Hoedl, E.; Kovacs, A.; Farnleitner, A.H. Long-term impact of basin-wide wastewater management on faecal pollution levels along the entire Danube River. *Environ. Sci. Pollut. Res.* **2024**, *31*, 45697–45710. [CrossRef] [PubMed]
30. Sefcik, K.; Speshock, J.; Brady, S.; Meik, J.M.; Brady, J.A. Tracking the Culprits: Microbial Source Tracking Uncovers Elevated Fecal Indicators along the Texas Coast. *Adv. Microbiol.* **2025**, *15*, 217–231. [CrossRef]
31. Steele, J.A.; González-Fernández, A.; Griffith, J.F.; Ebentier McCargar, D.; Wallace, S.; Schiff, K.C. Extrapolating empirical measurements of wastewater exfiltration from sanitary sewers to estimate watershed-scale fecal pollution loading in urban stormwater runoff. *Front. Environ. Sci.* **2025**, *12*, 1458153. [CrossRef]
32. Griffith, J.F.; Steele, J.A.; Gonzalez-Fernández, A.; Schiff, K.C. Towards quantifying exfiltration from in situ sanitary sewer pipes. *Front. Environ. Sci.* **2025**, *12*, 1458146. [CrossRef]
33. da Cruz Nizer, W.S.; Allison, K.N.; Adams, M.E.; Vargas, M.A.; Ahmed, D.; Beaulieu, C.; Raju, D.; Cassol, E.; Howell, P.L.; Overhage, J. The role of exopolysaccharides Psl and Pel in resistance of *Pseudomonas aeruginosa* to the oxidative stressors sodium hypochlorite and hydrogen peroxide. *Microbiol. Spectr.* **2024**, *12*, e0092224. [CrossRef]
34. Bao, Y.; Yang, B.; Yang, R.; Wang, J.; Geng, A.; Zhang, C.; Sun, Z. Regulation of microbial activity based on quorum sensing: Implications for biological wastewater treatment. *Int. Biodeterior. Biodegrad.* **2025**, *199*, 106029. [CrossRef]
35. Burt, A.; Cassidy, C.K.; Stansfeld, P.J.; Gutsche, I. Alternative Architecture of the *E. coli* Chemosensory Array. *Biomolecules* **2021**, *11*, 495. [CrossRef] [PubMed]
36. Das, I.; Das, S.; Das, S.; Ghangrekar, M.M. Proficient Sanitary Wastewater Treatment in Laboratory and Field-Scale Microbial Fuel Cell with Anti-Biofouling $Cu_{0.5}Mn_{0.5}Fe_2O_4$ as Cathode Catalyst. *J. Electrochem. Soc.* **2021**, *168*, 054519. [CrossRef]
37. Kharti, H.; Touach, N.; Lotfi, E.M.; El Mahi, M.; Mouhir, L.; Fekhaoui, M.; Benzaouak, A. Bioenergy generation and wastewater treatment with nickel pyrophosphate as a novel cathode catalyst in single-chamber microbial fuel cells. *Renew. Energy* **2024**, *231*, 121011. [CrossRef]